

Two parameter flow of $\sigma_{xx}(\omega) - \sigma_{xy}(\omega)$ for the graphene quantum Hall system in ac regime

Takahiro Morimoto and Hideo Aoki

Department of Physics, University of Tokyo, Hongo, Tokyo 113-0033, Japan

(Dated: November 12, 2018)

Flow diagram of $(\sigma_{xx}, \sigma_{xy})$ in finite-frequency (ω) regime is numerically studied for graphene quantum Hall effect (QHE) system. The ac flow diagrams turn out to show qualitatively similar behavior as the dc flow diagrams, which can be understood that the dynamical length scale determined by the frequency poses a relevant cutoff for the renormalization flow. Then the two parameter flow is discussed in terms of the dynamical scaling theory. We also discuss the larger- ω regime which exhibits classical flows driven by the raw frequency ω .

I. INTRODUCTION

In the quantum Hall effect (QHE), one standard and graphically clear way to grasp the physics involving the localization effect is the $\sigma_{xx} - \sigma_{xy}$ diagram, in which we look at the scaling flow (trajectories when the sample size is varied) of the longitudinal conductivity and Hall conductivity $(\sigma_{xx}, \sigma_{xy})$. The scaling property of the static QHE system, especially the quantization of the Hall conductivity into the multiples of e^2/h and vanishing longitudinal conductivity, is beautifully captured with the $\sigma_{xx} - \sigma_{xy}$ diagram as originally discussed by Pruisken and Khmelnitskii in terms of the non-linear sigma model¹⁻³. For the conventional two-dimensional electron gas (2DEG), there exist (i) stable fixed points at $(\sigma_{xx}, \sigma_{xy}) = (0, n)$ (n : integer), along with (ii) unstable fixed points characterizing delocalization at $(\sigma_{xx}, \sigma_{xy}) = (\sigma_{xx}^c, n + 1/2)$. The attraction into the former, quantum-Hall fixed point accounts for the Hall insulating state with quantized values of Hall conductivity, while the latter, unstable fixed point accounts for delocalized states at the center of each Landau level (LL), and dominates the behavior of the plateau-to-plateau transition in σ_{xy} .

Scaling properties of the Anderson transition have attracted both theoretical and experimental interests, since they should be universal and depend only on the symmetry class of the system⁴. The critical exponent has been numerically studied for the lowest LL⁵, and later with the Chalker-Coddington network model⁶ and experimentally confirmed by Li et al.⁷ The universal value of longitudinal conductances at the LL centers are intensively discussed with a tight binding lattice model⁸. Thus the scaling behavior at the plateau-to-plateau transition has been established.

On the other hand, rapid advances in the terahertz (THz) spectroscopy technique have made the optical responses of the quantum Hall system, such as cyclotron resonances and Faraday rotations, experimentally accessible^{9,10}. Specifically, the Faraday rotation is proportional to the optical Hall conductivity $\sigma_{xy}(\omega)$, and we have an intriguing problem of how the static Hall conductivity, which may be regarded as a topological quantity¹¹, evolves into the optical Hall conductivity, especially in the relevant (cyclotron) energy scale which falls upon

the THz regime.¹²⁻¹⁵ On the optical Hall conductivity, we have recently shown, numerically, that the plateau structure in $\sigma_{xy}(\omega)$ is unexpectedly retained in the ac (THz) regime in both 2DEG and in graphene, although the plateau height deviates from the quantized values in ac.¹⁴ Graphene is particularly interesting, since a massless Dirac system is realized as the low-energy physics, which accommodates a novel Dirac QHE is observed^{16,17}, for which the scaling theory of QHE in graphene has been formulated in terms of the non-linear sigma model¹⁸. Experimentally, the ac plateau has been observed in a GHz Faraday rotation measurement for a 2DEG system¹⁹ and recently in THz regime²⁰. In the graphene QHE system, we expect plateau structures at the tail (small frequency) region, while Faraday rotation was measured in the region around cyclotron resonances²¹.

Considering these advances in spectroscopies of QHE systems, it is important to study the systematic behavior of plateau structure in ac and optical regimes. Robustness of the ac plateau structure against disorder as revealed in the numerical result can be understood if we consider the effect of localization, which dominates the physics of electrons around the centers of Landau levels in disordered QHE systems, in finite-frequency regime, following the scaling theory of the Anderson transition. Namely, a finite frequency put an effective cutoff (the dynamical length scale L_ω) for the system, and the plateau in the ac Hall conductivity should be retained in the region where the localization length ($\xi \sim |\epsilon - \epsilon_c|^{-\nu}$) diverging toward LL center is smaller than the dynamically posed cutoff L_ω . In the two parameter flow picture, this can be viewed as the dynamical length scale L_ω determining a scale where the renormalization is stopped.

The dynamical scaling behavior has been studied for the ac longitudinal conductivity²², and for the optical Hall $\sigma_{xy}(\omega)$ ²³. Now, it is interesting to combine both the optical longitudinal and Hall $\sigma_{xy}(\omega)$ and numerically map out the two parameter $(\sigma_{xx} - \sigma_{xy})$ flow diagram in the ac regime.

In the present work we have calculated both optical longitudinal and Hall conductivities $(\sigma_{xx}, \sigma_{xy})$ for the graphene QHE system with a potential disorder, and combined them to numerically examine the two parameter $\sigma_{xx} - \sigma_{xy}$ flow diagram in the ac regime. We study

$n = 0$ LL in the graphene QHE system with exact diagonalization method to treat disorder effects. One particular point of interest is the behavior around fixed points in the $\sigma_{xx}(\omega) - \sigma_{xy}(\omega)$ diagram. There, we have focused on the $n = 0$ Dirac Landau level, where the peculiarity of graphene appears as the property that $n = 0$ is an electron-hole symmetric point. In a small- ω regime, we obtain numerical results which are coherent with the above picture that the $\sigma_{xx}(\omega) - \sigma_{xy}(\omega)$ flow obeys the Pruisken's two-parameter flow, with L_ω as a relevant cutoff for the system in ac region, where the flows are between $\sigma_{xy} = \pm 2e^2/h$ reflecting the graphene QHE including the valley and the spin degeneracies. We also discuss a large- ω regime where the frequency ω is comparable with the cyclotron frequency ω_c and exhibits classical flows driven by the raw frequency.

II. FORMALISM

For graphene QHE system, we employ the two-dimensional effective Dirac model,

$$H = v_F \tau_z \boldsymbol{\sigma} \cdot \boldsymbol{\pi} + V(\mathbf{r}), \quad (1)$$

where v_F is Fermi velocity, $\boldsymbol{\sigma} = (\sigma_x, \sigma_y)$ and τ_z the Pauli matrices acting on the space of two sublattices (A, B) and two valleys (K, K'), $\boldsymbol{\pi} = \mathbf{p} + e\mathbf{A}$ with $\mathbf{p} = (p_x, p_y)$ the momentum, and \mathbf{A} the vector potential. Disorder is introduced by a random potential,

$$V(\mathbf{r}) = \sum_{i,j} u_{i,j} \exp(-|\mathbf{r} - \mathbf{R}_{i,j}|^2/2d^2)/(2\pi d^2),$$

composed of Gaussian scattering centers of range d and $u_{i,j}$ takes a value in $(-u, u)$ randomly. Here we take $d = 0.7\ell$, where $\ell = \sqrt{\hbar/eB}$ is the magnetic length. For numerical facility, impurity sites $R_{i,j}$ are periodically placed on $R_{i,j} = (2\pi\ell^2/L)(i, j)$ with L being the linear dimension of the sample. A measure of disorder is given by the Landau level broadening²⁴, $\Gamma = 2u[N_{imp}/2\pi(\ell^2 + 2d^2)L^2]^{1/2}$, with a number of impurity sites N_{imp} . We assume smooth potential disorders in the length scale of underlying lattice structure, and we neglect inter-valley scattering. The cyclotron energy is, for a Dirac particle, given by $\omega_c = \sqrt{2}v_F/\ell$.

Since we are interested in the dynamical $\sigma_{xx}(\omega) - \sigma_{xy}(\omega)$, which should be related to the localization physics, we obtain the eigenstates of the Hamiltonian with an exact diagonalization, which is done for a subspace spanned by a finite number of Landau levels (LL's) around $n = 0$ LL, for $L \times L$ systems with L/ℓ varied over 20, 30, 40. Here we retain 5 LLs ($n = -2 \sim 2$), which poses an ultraviolet cutoff.³⁷ In the Landau gauge $\mathbf{A} = (0, Bx)$, the basis function is $\psi_{n,k} = e^{-iky} \phi_n(x - \ell^2 k_y)$, where ϕ_n is the Dirac-Landau function in the n -th Landau level²⁵, and wavenumbers k takes an integer multiples of $2\pi/L$ with a periodic boundary condition for y -direction. The number of discrete wavenumbers N_k is

related to L with $N_k = L^2/2\pi\ell^2$ in a finite system. From the eigenfunctions ψ_a and eigenenergies ϵ_a obtained with the exact diagonalization, the optical Hall conductivity¹⁴ is evaluated from the Kubo formula²⁶ as

$$\sigma_{xy}(\omega) = \frac{\hbar}{iL^2} \sum_{ab} j_x^{ab} j_y^{ba} \frac{f(\epsilon_b) - f(\epsilon_a)}{\epsilon_b - \epsilon_a} \frac{1}{\epsilon_b - \epsilon_a - \hbar\omega - i\eta}, \quad (2)$$

where $f(\epsilon)$ is the Fermi distribution, and η a low-energy cutoff. The current matrix element, j_x^{ab} , has a selection rule peculiar to Dirac model ($n \leftrightarrow \pm n \pm 1$ with n the Landau index), which is distinct from that ($n \leftrightarrow n \pm 1$) for 2DEG as

$$j_x^{n,n'} = ev_F C_n C_{n'} [\text{sgn}(n)\delta_{|n|-1,|n'|} + \text{sgn}(n')\delta_{|n|+1,|n'|}], \\ j_y^{n,n'} =iev_F C_n C_{n'} [\text{sgn}(n)\delta_{|n|-1,|n'|} - \text{sgn}(n')\delta_{|n|+1,|n'|}],$$

where $C_n = 1(n = 0)$ or $1/\sqrt{2}$ (otherwise)^{25,27}.

The longitudinal conductivity, on the other hand, is given by

$$\text{Re}\sigma_{xx}(\omega) = \frac{\hbar}{L^2} \sum_{\epsilon_a, \epsilon_b} \frac{f(\epsilon_b) - f(\epsilon_a)}{\epsilon_b - \epsilon_a} \frac{|j_x^{ab}|^2 \eta}{(\epsilon_b - \epsilon_a - \hbar\omega)^2 + \eta^2}.$$

We note that the low-energy cutoff η , which affects the $\omega \sim 0$ behavior of $\sigma_{xx}(\omega)$, should be chosen close to the Thouless energy, which is typically of the order of the energy level spacing $\sim 1/L^2$.²⁸⁻³⁰ The temperature in the Fermi distribution function $f(\epsilon)$ is set to be small as far as the low-frequency behavior of $\sigma_{xx}(\omega)$ is numerically stable, which is achieved if we put the temperature to be of the order of the level spacing $\sim 1/L^2$. For the scaling analysis the calculation is repeated for varied sample size L , Fermi energy ϵ_F and frequency ω . Throughout the paper the length, energy and frequency are respectively in units of ℓ , $\hbar\omega_c$ and ω_c .

III. $\sigma_{xx} - \sigma_{xy}$ DIAGRAM IN AC REGIME

First we discuss the behavior $\sigma_{xx}(\omega)$ and $\sigma_{xy}(\omega)$ separately. $\sigma_{xx}(\epsilon_F, \omega)$ in Fig.1(a) shows a ridge structure along the ω axis when the Fermi energy ϵ_F is around the delocalized region at each LL. When we increase L in Fig.1(b), the width of $\sigma_{xx}(\omega = 0)$ becomes narrower, while the peak height stays almost constant which is expected from the universal longitudinal conductance^{8,31,32}. On the other hand, $\sigma_{xy}(\epsilon_F, \omega)$ plotted against ϵ_F in Fig.1(c) shows a transition from $\sigma_{xy} = -2$ plateau to $\sigma_{xy} = 2$ plateau around $n = 0$ LL with 2 valley and 2 spin degeneracies, where the transition width of $\sigma_{xy}(\omega = 0)$ sharpens with increasing L .

Now we are in a position to examine $\sigma_{xx} - \sigma_{xy}$ diagram in Fig.2. First, the diagram for $\omega = 0$ is depicted in Fig.2(a), where almost all the points are attracted to the points $(\sigma_{xx}, \sigma_{xy}) = (0, \pm 2)e^2/h$ with increased sample size L , while the point sitting at $\sigma_{xy} = 0$ only

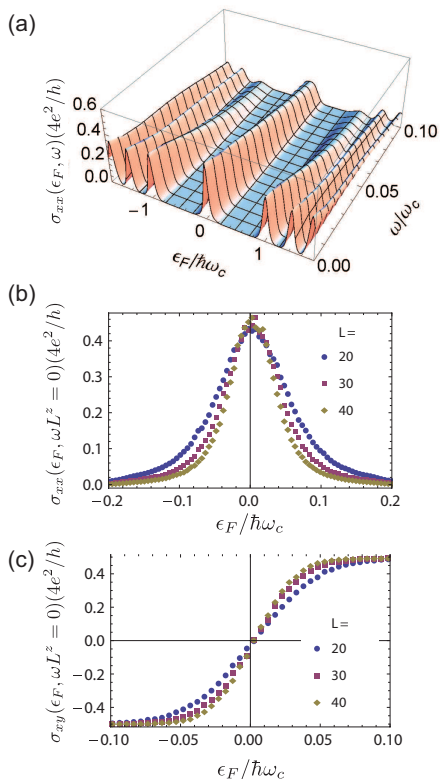


FIG. 1: (a) $\sigma_{xx}(\epsilon_F, \omega)$ plotted against the Fermi energy ϵ_F and the frequency ω for $L = 30$. Lower panels depict $\sigma_{xx}(\omega = 0)$ (b) and $\sigma_{xy}(\omega = 0)$ (c) for various sample sizes with disorder strength $\Gamma/\hbar\omega_c = 0.4$.

exhibits a tiny, upward flow. This numerically calculated dc flow diagram is clearly understood in terms of Pruisken's two parameter flow picture¹⁻³. We can interpret the static result that the flows starting from $\sigma_{xy} \neq 0$ corresponding to those flowing into the stable fixed points at $(\sigma_{xx}, \sigma_{xy}) = (0, \pm 2)e^2/h$ which describes Hall plateau for graphene, while the tiny upward flow around $\sigma_{xy} = 0$ corresponds to the flow that starts from the point with a σ_{xx} smaller than σ_{xx}^c (rather than larger σ_{xx} expected from SCBA values), and shows a renormalization to the unstable fixed point at $(\sigma_{xx}, \sigma_{xy}) = (\sigma_{xx}^c, 0)$. So we are seeing the region below the unstable fixed point. This upward flow toward the unstable fixed point would reflect the existence of the delocalized state at the LL center, since it is percolating through the sample and has a metallic nature. The longitudinal conductivity then increases with the sample size and converges to the universal conductance at the LL center. This dc result for graphene $n = 0$ LL is consistent with Nomura et al who discusses the Thouless-number and the Hall conductivity for the dc flow diagram.³⁰

If we now turn to the ac result that is plotted for a fixed system size $L/\ell = 30$ varying frequency $\omega/\omega_c = 0.0025 \sim 0.015$ in Fig.2(b), where a behavior quite similar to the dc

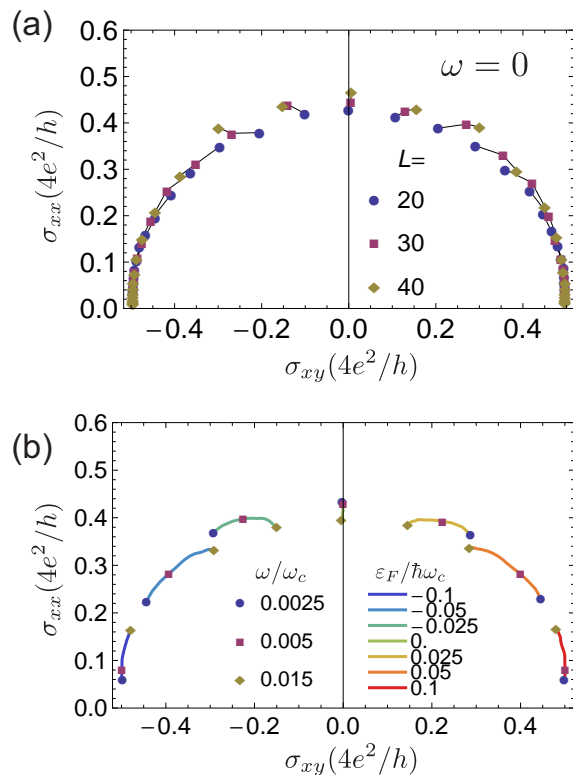


FIG. 2: The flow of $(\sigma_{xx}(\omega) - \sigma_{xy}(\omega))$ in the graphene quantum Hall system with a disorder strength $\Gamma/\hbar\omega_c = 0.4$. (a) The flow in dc regime ($\omega = 0$) for various Fermi energy ϵ_F and system size $L/\ell = 20, 30, 40$. (b) The flow in ac regime for various values of Fermi energy ϵ_F and frequency ω with a fixed system size $L/\ell = 30$

data is found. Namely, almost all the points away from the LL center are attracted to the QHE fixed points, while the point on $\sigma_{xy} = 0$ at the center of LL flows only slightly shift upwards. This behavior is understood that, in this small frequency regime, the relevant cutoff length scale for the critical behavior of localization length ξ or the renormalization equation for two-parameter flow is posed by the frequency through the dynamical length scale L_ω instead of the sample size L in the dc regime, so that the overall behavior is determined by the same two-parameter flow, where the effective cutoff alone is changed systematically with the frequency ω as $L_\omega \sim \omega^{-1/z}$.

IV. DYNAMICAL SCALING ANALYSIS

Now let us describe the dynamical scaling for $\sigma_{xx}(\epsilon_F, \omega)$ and $\sigma_{xy}(\epsilon_F, \omega)$. The scaling argument starts from an ansatz that the optical conductivity depends on Fermi energy ϵ_F and frequency ω only through the ratios L/ξ and L_ω/ξ . The physical quantities should then be described in terms of the universal scaling function of

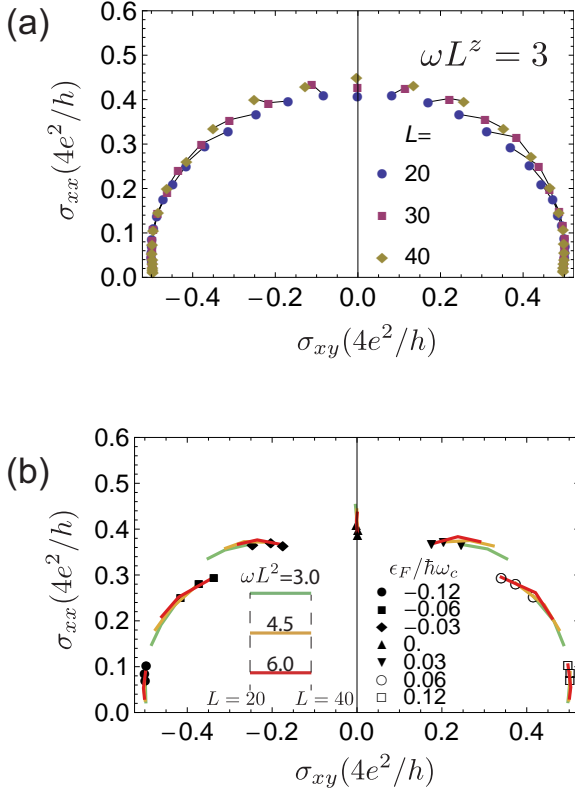


FIG. 3: (a) The flow of $(\sigma_{xx}(\omega) - \sigma_{xy}(\omega))$ in the graphene quantum Hall system for renormalized frequency $\omega L^z = 3$ with $z = 2$ and $L = 20, 30, 40$ with a disorder strength $\Gamma/\hbar\omega_c = 0.4$. (b) Flows when the sample size is varied as $L = 20 \rightarrow 40$ for a fixed of ωL^z . For each value of ωL^z we plot the flows corresponding to various values of Fermi energy ϵ_F . The value of ϵ_F is indicated by different symbols (circles, squares, etc) that mark the smallest sample size ($L = 20$). The results for various values (color-coded) of $\omega L^z = 3 - 6$ are superposed.

the ratios L/ξ and L_ω/ξ . Here ξ is the localization length with a critical behavior $\xi \sim 1/|\epsilon_F - \epsilon_c|^\nu$, where ϵ_c is the critical energy which coincides with the center of the LL ($\epsilon_c = 0$ for $n = 0$), and ν the localization critical exponent. The dynamical length scale, which is the distance over which an electron travels during one cycle, $1/\omega$, of the ac field, is assumed to behave as $L_\omega \sim 1/\omega^{1/z}$, where z is the dynamical critical exponent, assuming $z = 2$ in this paper since we treat the non-interacting electrons³³, while $z = 1$ is established for the case with electron-electron interaction³⁴. For these critical behaviors the dynamical scaling ansatz for the longitudinal and transverse conductivities amounts to³⁵

$$\begin{aligned}\sigma_{xx}(\epsilon_F, \omega, L) &= \frac{e^2}{h} F_{xx}(\delta\epsilon_F L^{1/\nu}, \omega L^z), \\ \sigma_{xy}(\epsilon_F, \omega, L) &= \frac{e^2}{h} F_{xy}(\delta\epsilon_F L^{1/\nu}, \omega L^z),\end{aligned}\quad (3)$$

where F_{xx}, F_{xy} are universal scaling functions, and $\delta\epsilon_F \equiv \epsilon_F - \epsilon_c$.

This ansatz is only valid for the critical region, where the deviation of Fermi energy from the LL center $\delta\epsilon_F$ is assumed to be small and the frequency ω also to be small. In Sec.3 and Sec.4, we precisely consider this region with small $\delta\epsilon_F$ and ω , while in Sec.5 where we shall treat a large-frequency region this ansatz should be no longer applicable. The ansatz indicates that the flow of $(\sigma_{xx}(\omega), \sigma_{xy}(\omega))$ in the ac region depends on the frequency ω only through the ratio of the rescaled frequency with the system size as ωL^z .

We now interpret the behavior of $\sigma_{xx} - \sigma_{xy}$ diagram in terms of the dynamical scaling eqn.(3) as shown in Fig.3. When we consider a dynamical scaling behavior, it is convenient to consider a rescaled frequency ωL^z since a dependence on the frequency appears in a form of ωL^z in eqn.(3). In Fig. 3(a) we show a result for a fixed rescaled frequency $\omega L^z = 3$, then the flow of ac conductivities can be discussed in terms of varying L as in dc case. The dynamical scaling hypothesis (eqn.(3)) expects that $(\sigma_{xx}, \sigma_{xy})$ right on $\epsilon_F = 0$ with $\delta\epsilon_F L^{1/\nu} = 0$ for all L should depend only on ωL^z , i.e., does not flow, while at the center of Fig.3(a) a slight upward flow is seen showing a metallic behavior discussed above. Away from $\epsilon_F = 0$, on the other hand, the flow should depend only on $\delta\epsilon_F L^{1/\nu}$ from eq.(3) for a fixed value of the rescaled frequency ωL^z , which implies that the flows starting from various $\epsilon_F \neq 0$ should reside on a single curve as seen in Fig.3(a).

In order to examine the dependence of the two parameter flow on the rescaled frequency ωL^z , we superpose all the results in Fig.3(b). There, we show flows when the sample size is varied as $L = 20 \rightarrow 40$ for fixed values of ωL^z . For each value of ωL^z we plot the flows corresponding to various values of Fermi energy ϵ_F . The value of ϵ_F is indicated by different symbols that mark the smallest sample size ($L = 20$). Fig.3(b) thus visualizes the two-parameter flows superposes for various values of ωL^z and for various values of Fermi energy ϵ_F . The results for various values of $\omega L^z = 3 - 6$ are then superposed in Fig.3(b). In this summary plot we can see that the $(\sigma_{xx}, \sigma_{xy})$ flows for different values of ωL^z tend to coalesce into a single curve in the region away from $\sigma_{xy} = 0$. This is a consequence that we see the same two parameter flow with various cutoff length scale posed by different rescaled frequencies. Close to the unstable fixed point at $(\sigma_{xx}, \sigma_{xy}) = (\sigma_{xx}^c, 0)$ the flow shows a metallic behavior (i.e., σ_{xx} increasing with L) renormalizing into the unstable fixed point with increasing σ_{xx} , and slightly deviates from a single curve. The role of the value of increasing ωL^z appears in a shift of the initial position of the flow in $(\sigma_{xx}(\omega), \sigma_{xy}(\omega))$ for each ϵ_F toward the opposite direction to the flow. More precisely, for a larger ωL^z we have more broadened peak structure in σ_{xx} and more broadened transition width in σ_{xy} , so that the initial point (smallest- L data) of the flow for each ϵ_F shifts closer to the unstable fixed point (the center of the flow

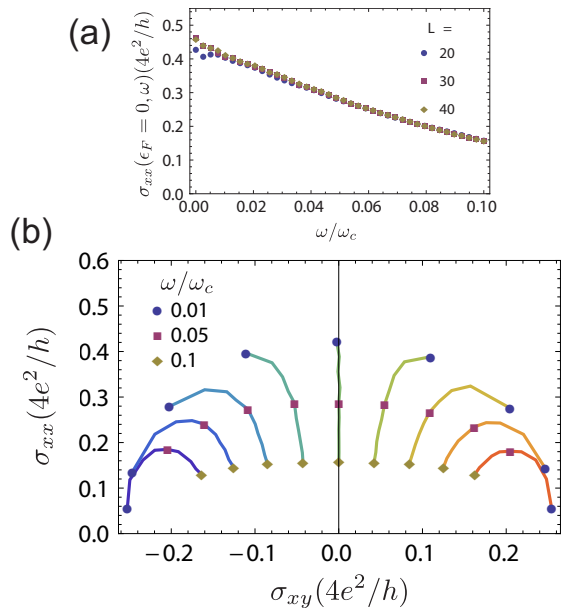


FIG. 4: (a) $\sigma_{xx}(\epsilon_F = 0, \omega)$ plotted for frequency up to $\omega = 0.1$, where the data for various system sizes almost coincide with each other for large ω . (b) $\sigma_{xx}(\omega) - \sigma_{xy}(\omega)$ diagram for raw frequency ω with $L = 30$.

at $(\sigma_{xx}, \sigma_{xy}) = (\sigma_{xx}^c, 0)$, which we can observe in a shift of initial values in Fig.3(b). This behavior arises from the fact that the relevant cutoff for the two-parameter flow in the ac regime is determined by the dynamical length scale L_ω , where a larger frequency ω gives a smaller cutoff length scale $L_\omega \sim \omega^{-1/z}$ and leads to an overall shift toward the direction opposite to that of the flow (in this case, toward the unstable fixed point), and a more broadened width of the plateau-to-plateau transition.

V. FLOW DIAGRAMS FOR LARGER ω

So far we have discussed the behavior for a small-frequency region, where the dynamical length scale $L_\omega \sim \omega^{-1/z}$ behaves an infrared cutoff for the critical phenomena at the Anderson transition and the dynamical scaling arguments also hold quite well. It is worth while to ask how the behavior of the larger-frequency region, typically for ω up to $0.1\omega_c$, looks like in a similar two-parameter $\sigma_{xx} - \sigma_{xy}$ plot. Naturally, in the large-frequency region, ac conductivities are expected to be no longer dominated by the criticality and show a qualitatively dif-

ferent, rather classical behavior. In this region we should adopt raw ω instead of ωL^z , because the system should be out of the critical (i.e., dynamical-scaling) region. In Fig.4(a), we look at the large- ω behavior of the longitudinal $\sigma_{xx}(\omega, \epsilon_F = 0)$ against the frequency ω , from $\omega = 0.01\omega_c$ to $\omega = 0.1\omega_c$. In a large-frequency, ac longitudinal conductivity at the center of LL shows a monotonic decrease of $\sigma_{xx}(\epsilon = 0)$ with ω as consistent with Ref.²². This clearly signals a deviation from the dynamical scaling ansatz, which assumes the ωL^z -dependent conductivity as in eqn.3.

The $\sigma_{xx}(\omega) - \sigma_{xy}(\omega)$ diagram for the large- ω region where the flows are indicated with varying frequency ω for various values of ϵ_F is shown in Fig.4(b). The ω -driven flows show a different pattern from the flows in a small- ω region in the previous section, although it is attracted with decreasing ω to the static-QHE fixed points $(\sigma_{xx}, \sigma_{xy}) = (0, \pm 2)e^2/h$, just as in the temperature-driven flows³⁶. This behavior is understood that in the large-frequency region, where frequency ω become comparable to the cyclotron frequency ω_c , the frequency puts a small length scale comparable to the magnetic length, which should naturally induce deviations from the critical region and show a pattern of the two conductivities different from that in the small-frequency region. The existence itself of flows around $\omega/\omega_c \sim 1$ implies that the system is not fully dominated by a Drude-like behavior, which is consistent with the observation of the ac plateau structure in this frequency region, i.e., $\omega \sim 0.1$ that corresponds to the THz region.

VI. SUMMARY

We have numerically obtained $\sigma_{xx}(\omega) - \sigma_{xy}(\omega)$ diagram for graphene QHE system, and have examined the flow for two regimes. In a small- ω regime, flows are governed by the dynamical length scale posed by the frequency as a relevant cutoff length scale for the criticality around the Anderson transition. We also discussed a metallic behavior around the unstable fixed point reflecting the delocalized state at the LL center. The larger- ω regime exhibits rather classical flows driven by the bare frequency due to the small dynamical length scale comparable to the magnetic length scale.

We wish to thank Mikito Koshino, Kentaro Nomura and Akira Furusaki for illuminating discussions. This work has been supported in part by Grants-in-Aid for Scientific Research, Nos.20340098, 23340112 from JSPS. TM has been supported by JSPS.

¹ A. M. M. Pruisken, Phys. Rev. Lett. **61**, 1297 (1988).

² A. M. M. Pruisken, Phys. Rev. B **32**, 2636 (1985).

³ D. Khmel'nitskii, JETP. Lett **38**, 552 (1983).

⁴ B. Huckestein, Rev. Mod. Phys. **67**, 357 (1995).

⁵ B. Huckestein and B. Kramer, Phys. Rev. Lett. **64**, 1437 (1990).

⁶ K. Slevin and T. Ohtsuki, Phys. Rev. B **80**, 041304 (2009).

⁷ W. Li, C. L. Vicente, J. S. Xia, W. Pan, D. C. Tsui, L. N.

- Pfeiffer, and K. W. West, Phys. Rev. Lett. **102**, 216801 (2009).
- ⁸ L. Schweitzer and P. Markoš, Phys. Rev. Lett. **95**, 256805 (2005).
- ⁹ H. Sumikura, T. Nagashima, H. Kitahara, and M. Hangyo, Jpn. J. Appl. Phys. **46**, 1739 (2007).
- ¹⁰ Y. Ikebe and R. Shimano, Appl. Phys. Lett. **92**, 012111 (2008).
- ¹¹ D. J. Thouless, M. Kohmoto, M. P. Nightingale, and M. den Nijs, Phys. Rev. Lett. **49**, 405 (1982).
- ¹² V. Volkov and S. Mikhailov, JETP Letters **41**, 476 (1985).
- ¹³ V. P. Gusynin, S. G. Sharapov, and J. P. Carbotte, Journal of Physics: Condensed Matter **19**, 026222 (2007).
- ¹⁴ T. Morimoto, Y. Hatsugai, and H. Aoki, Phys. Rev. Lett. **103**, 116803 (2009).
- ¹⁵ I. V. Fialkovsky and D. V. Vassilevich, J. Phys. A: Math. Theor. **42**, 442001 (2009).
- ¹⁶ K. Novoselov, A. Geim, S. Morozov, D. Jiang, M. Katsnelson, I. Grigorieva, S. Dubonos, and A. Firsov, Nature **438**, 197 (2005).
- ¹⁷ Y. Zhang, Y. Tan, H. Stormer, and P. Kim, Nature **438**, 201 (2005).
- ¹⁸ P. M. Ostrovsky, I. V. Gornyi, and A. D. Mirlin, Phys. Rev. B **77**, 195430 (2008).
- ¹⁹ F. Hohls, U. Zeitler, R. Haug, R. Meisels, K. Dybko, and F. Kuchar, Phys. Rev. Lett. **89**, 276801 (2002).
- ²⁰ Y. Ikebe, T. Morimoto, R. Masutomi, T. Okamoto, H. Aoki, and R. Shimano, Phys. Rev. Lett. **104**, 256802 (2010).
- ²¹ I. Crassee, J. Levallois, A. Walter, M. Ostler, A. Bostwick, E. Rotenberg, T. Seyller, D. Van Der Marel, and A. Kuzmenko, Nat. Phys. **7**, 48 (2011).
- ²² B. M. Gammel and W. Brenig, Phys. Rev. B **53**, R13279 (1996).
- ²³ T. Morimoto, Y. Avishai, and H. Aoki, Phys. Rev. B **82**, 081404 (2010).
- ²⁴ T. Ando, J. Phys. Soc. Jpn. **38**, 989 (1975).
- ²⁵ Y. Zheng and T. Ando, Phys. Rev. B **65**, 245420 (2002).
- ²⁶ R. Kubo, S. J. Miyake, and N. Hashitsume (Academic Press, 1965), vol. 17 of *Solid State Physics*, pp. 269 – 364.
- ²⁷ N. Shon and T. Ando, J. Phys. Soc. Japan **67**, 2421 (1998).
- ²⁸ D. Thouless and S. Kirkpatrick, J. Phys. C **14**, 235 (1981).
- ²⁹ K. Nomura, M. Koshino, and S. Ryu, Phys. Rev. Lett. **99**, 146806 (2007). ; K. Nomura and N. Nagaosa, Phys. Rev. Lett. **106**, 166802 (2011).
- ³⁰ K. Nomura, S. Ryu, M. Koshino, C. Mudry, and A. Furusaki, Phys. Rev. Lett. **100**, 246806 (2008).
- ³¹ S. Kivelson, D.-H. Lee, and S.-C. Zhang, Phys. Rev. B **46**, 2223 (1992).
- ³² L. W. Wong, H. W. Jiang, N. Trivedi, and E. Palm, Phys. Rev. B **51**, 18033 (1995).
- ³³ B. Huckestein and M. Backhaus, Phys. Rev. Lett. **82**, 5100 (1999).
- ³⁴ D. G. Polyakov and B. I. Shklovskii, Phys. Rev. B **48**, 11167 (1993).
- ³⁵ Z. Wang, M. P. A. Fisher, S. M. Girvin, and J. T. Chalker, Phys. Rev. B **61**, 8326 (2000).
- ³⁶ H. Aoki and T. Ando, Surf. Sci. **170**, 249 (1986).
- ³⁷ For each valley, this choice of high-energy cutoff (retaining $n = -N_{max} \sim N_{max}$ LLs) makes the Hall conductivity coincide with the half of the total Hall conductivity contributed from both two valleys (K, K'), for which a cancellation of a ultraviolet divergence occurs¹⁸. So we can concentrate on one of the decoupled valleys in the numerical calculation, although well-defined conductivities are the sum of contributions from two valleys